JACS
JOURNAL OF THE AMERICAN CHEMICAL SOCIETY

Article

pubs.acs.org/JACS

Elucidating the Breathing of the Metal–Organic Framework MIL-53(Sc) with ab Initio Molecular Dynamics Simulations and in Situ X-ray Powder Diffraction Experiments

Linjiang Chen,[†] John P. S. Mowat,[‡] David Fairen-Jimenez,[§] Carole A. Morrison,[∥] Stephen P. Thompson,[⊥] Paul A. Wright,[‡] and Tina Düren*[,†]

[†]Institute for Materials and Processes, School of Engineering, The University of Edinburgh, King's Buildings, Edinburgh EH9 3JL, United Kingdom

[‡]EaStCHEM School of Chemistry, University of St. Andrews, Purdie Building, North Haugh, St. Andrews, Fife KY16 9ST, United Kingdom

[§]Department of Chemical Engineering and Biotechnology, University of Cambridge, Pembroke Street, Cambridge CB2 3RA, United Kingdom

[∥]EaStCHEM Research School, The University of Edinburgh, King's Buildings, Edinburgh EH9 3JJ, United Kingdom

[⊥]Diamond Light Source Ltd., Harwell Science and Innovation Campus, Didcot, Oxfordshire OX11 0DE, United Kingdom

Supporting Information

ABSTRACT: Ab initio molecular dynamics (AIMD) simulations have been used to predict structural transitions of the breathing metal–organic framework (MOF) MIL-53(Sc) in response to changes in temperature over the range 100–623 K and adsorption of CO_2 at 0–0.9 bar at 196 K. The method has for the first time been shown to predict successfully both temperature-dependent structural changes and the structural response to variable sorbate uptake of a flexible MOF. AIMD employing dispersion-corrected density functional theory accurately simulated the experimentally observed closure of MIL-53(Sc) upon solvent removal and the transition of the empty MOF from the *closed-pore* phase to the *very-narrow-pore* phase (symmetry change from $P2_1/c$ to $C2/c$) with increasing temperature, indicating that it can directly take into account entropic as well as enthalpic effects. We also used AIMD simulations to mimic the CO_2 adsorption of MIL-53(Sc) in silico by allowing the MIL-53(Sc) framework to evolve freely in response to CO_2 loadings corresponding to the two steps in the experimental adsorption isotherm. The resulting structures enabled the structure determination of the two CO_2-containing *intermediate* and *large-pore* phases observed by experimental synchrotron X-ray diffraction studies with increasing CO_2 pressure; this would not have been possible for the *intermediate* structure via conventional methods because of diffraction peak broadening. Furthermore, the strong and anisotropic peak broadening observed for the *intermediate* structure could be explained in terms of fluctuations of the framework predicted by the AIMD simulations. Fundamental insights from the molecular-level interactions further revealed the origin of the breathing of MIL-53(Sc) upon temperature variation and CO_2 adsorption. These simulations illustrate the power of the AIMD method for the prediction and understanding of the behavior of flexible microporous solids.

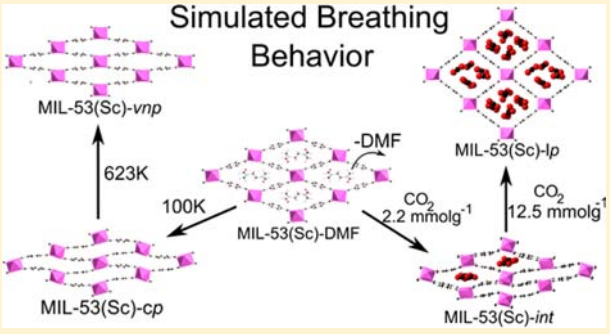

1. INTRODUCTION

Metal–organic frameworks (MOFs)[1] (also known as porous coordination polymers[2]) are hybrid porous solids that represent an extensive family of crystalline materials realized through modular syntheses from metal centers and organic ligands. Breathing MOFs combine "regularity" with "softness" by exhibiting large, reversible structural deformations (softness) upon the action of various external physical (e.g., temperature or mechanical pressure) or chemical (e.g., guest-molecule inclusion) stimuli without loss of crystallinity or bond breaking (regularity).[3,4] This phenomenon is characterized by pronounced reversible structural transitions between two (or more) states resulting from the expansion or contraction of the three-dimensional porous framework. The associated large variations in unit cell volume, sometimes as much as 40–270%,[5,6] give rise to promising applications of these breathing MOFs in numerous fields ranging from gas storage and separation to drug encapsulation and delivery.[7,8]

Among these soft porous solids, the trivalent metal (M^{3+}; M = Cr, Al, Fe, Sc, etc.) terephthalate MIL-53 ("MIL" stands for Materials of Institute Lavoisier) is one of the most widely

Received: April 7, 2013
Published: June 3, 2013

   dx.doi.org/10.1021/ja403453g | J. Am. Chem. Soc. 2013, 135, 15763–15773

studied of all MOFs because of its ability to change crystal structure markedly in response to changes in temperature and guest-molecule adsorption (Figure 1).[5,9−11] The compounds

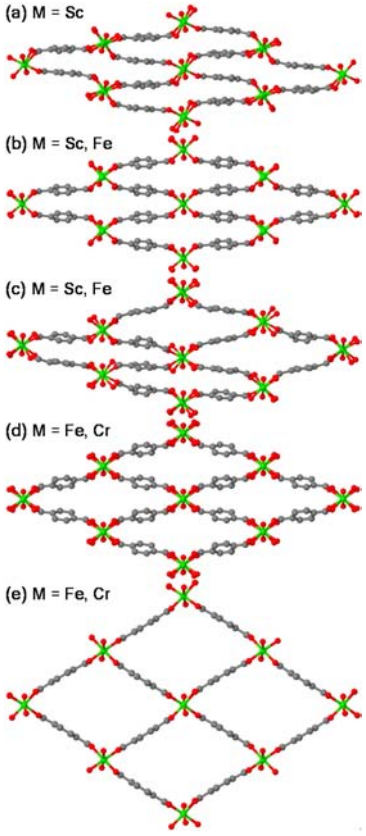

Figure 1. Schematic representation, together with examples, of the different structural forms of MIL-53 observed for different metals: (a) *cp*; (b) *vnp*; (c) *int*; (d) *np*; and (e) *lp*. Color code: gray, carbon; red, oxygen; green, metal.

belonging to the MIL-53 family are built up from chains of μ_2-OH corner-sharing $MO_4(OH)_2$ octahedra linked via terephthalate linkers to define a three-dimensional ordered network with one-dimensional diamond-shaped channels. One intriguing feature of the MIL-53 family is the dramatically different breathing behaviors observed for different M^{3+} centers. The MIL-53(Cr) solid,[5] for example, exhibits either an orthorhombic *large-pore* (*lp*) form (Figure 1e) that is favored by dehydration, higher temperatures, and larger adsorbate uptakes or a monoclinic *narrow-pore* (*np*) form (Figure 1d) found at lower temperatures and lower uptakes. The iron analogue MIL-53(Fe) shows more complex breathing behavior,[12,13] with the dehydrated material adopting a *very-narrow-pore* (*vnp*) form with *C*2/*c* symmetry (Figure 1b) that takes up CO_2 to give an *intermediate* (*int*) form (Figure 1c) before opening sequentially to give the *np* (Figure 1d) and *lp* (Figure 1e) forms.

Our own studies of the scandium analogue[11,14] indicated similarly complex but crystallographically distinct breathing behavior in response to solvent removal, temperature variation, and adsorption of H_2O and CO_2. Upon removal of occluded dimethylformamide (DMF) solvent from the as-prepared form, MIL-53(Sc) does not open but instead contracts to give a *closed-pore* (*cp*) form with $P2_1/c$ symmetry (Figure 1a) that is distinct from the *vnp* form (Figure 1b) and without accessible porosity to N_2 or CO_2. MIL-53(Sc) is observed to be in the *cp* form from 100−573 K with a gradual expansion in the unit cell volume in response to increasing temperature; by 623 K it has undergone a transition to a *vnp* form with C2/*c* symmetry that is isostructural to MIL-53(Fe)-*vnp*.[13] This change is fully reversible with decreasing temperature. The transition complexity of MIL-53(Sc) goes beyond this sensitive response to temperature variation. Hydration of MIL-53(Sc)-*cp* at room temperature, for example, leads to MIL-53(Sc)-H_2O in an *int* phase having triclinic symmetry (Figure 1c) in which half of the channels are partially open as a result of the uptake of water molecules while the others are empty and closed.[11] The CO_2 adsorption isotherm of MIL-53(Sc)[11,14] is different from those reported for MIL-53(Cr) and MIL-53(Fe): an initial region of zero uptake is followed by two steps, the first at 2−3 mmol g^{-1} and the second at 13 mmol g^{-1}. The latter is attributed to full opening to the *lp* form (Figure 1e), as observed for various solids of the MIL-53 structure type upon uptake of large amounts of adsorbates.[5,9,15,16] However, no in situ diffraction data were available to confirm the presence of the *lp* form or to establish the structure responsible for the uptake of 2−3 mmol/g of CO_2.

A considerable number of multidisciplinary studies have been devoted to understanding the structural transformations observed for breathing MOFs of the MIL-53 type and others.[16−21] In particular, MIL-53(Cr), a textbook example of a bistable (i.e., *lp* ⇄ *np* transition) breathing MOF, has been extensively explored. Some well-established experimental methods that have routinely been deployed include (1) manometric/gravimetric and microcalorimetric measurements for studying a variety of adsorbate molecules; (2) in situ techniques (e.g., X-ray diffraction, IR or Raman spectroscopy) used, for example, to locate adsorbates in the pores or probe the nature of adsorption sites; and (3) quasi-elastic neutron scattering experiments to help with understanding the dynamics of a probe molecule in a host MOF.[7,22] Hand-in-hand with the experimental efforts, theoretical investigations of breathing MOFs on different length and/or time scales have also been carried out.[23−27] The richness of the insights provided by computational methodologies spans from mechanistic details realized through a quantum-mechanical (QM) description of the electronic structure of the system[13,28] [primarily relying on static density functional theory (DFT) calculations] to macroscopic thermodynamic information on the sample level, which can provide insight into, for instance, the interplay between the adsorbent elasticity and guest molecule adsorption.[27,29] In particular, force-field-based molecular simulation studies, including both Monte Carlo (MC) and molecular dynamics (MD) methods,[30] have made substantial contributions toward elucidating the microscopic mechanisms that govern the structural deformations.[17,21,23,24,31−36]

MD simulations are particularly suited to coupling with experiment to study MOF breathing phenomena because they offer a detailed description of the system of interest on the atomic/molecular level. As an MD simulation reveals points in phase space that are connected in time, it can provide an evolving picture of the breathing behavior that readily conveys valuable details on, for instance, how cooperative movements of the framework ligands, together with the interactions between the inorganic and organic moieties, facilitate the major structural changes of the MIL-53 solids.[3,31] Moreover, information concerning the kinetics and energetics of the breathing motion can be extracted from MD simulations to help reveal collective effects of the guest−guest, guest−host,

dx.doi.org/10.1021/ja403453g | J. Am. Chem. Soc. 2013, 135, 15763−15773

Table 1. Comparison of AIMD-Simulated and Experimental (in Parentheses)[a] Unit Cell Parameters for the *cp* (100 and 293 K) and *vnp* (623 K) Forms of MIL-53(Sc)

T (K)	a (Å)	b (Å)	c (Å)	α (deg)	β (deg)	γ (deg)	V (Å^3)
100.00	20.22 ± 0.08	7.44 ± 0.04	11.35 ± 0.06	90.00 ± 0.55	103.60 ± 0.52	90.00 ± 0.40	1658.18 ± 7.82
	(20.30)	*(7.33)*	*(11.69)*	*(90.00)*	*(104.96)*	*(90.00)*	*(1680.75)*
293.00	20.33 ± 0.14	7.44 ± 0.08	11.48 ± 0.13	90.00 ± 1.15	104.07 ± 1.09	90.00 ± 0.83	1684.89 ± 16.98
	(20.33)	*(7.33)*	*(11.84)*	*(90.00)*	*(105.21)*	*(90.00)*	*(1701.36)*
623.00	20.04 ± 0.13	7.42 ± 0.20	13.12 ± 0.15	89.58 ± 3.25	90.25 ± 2.17	90.36 ± 2.39	1950.77 ± 43.39
	(19.71)	*(7.27)*	*(13.26)*	*(90.00)*	*(90.00)*	*(90.00)*	*(1901.65)*
starting[b]	*(19.34)*	*(7.30)*	*(18.36)*	*(90.00)*	*(90.00)*	*(90.00)*	*(2593.16)*

[a]Experimental data were taken from the work of Mowat et al.[14] [b]The experimental MIL-53(Sc)-*DMF(removed)* structure[11] was used as the starting configuration for the simulations at the three temperatures.

and sometimes host−host interactions. To date, most of the reported MD studies aimed at capturing the breathing phenomena of MOFs have made use of flexible force fields tailor-made for the frameworks. Such force fields are usually obtained either by employing accurate QM calculations[37] or via a combination of chemical intuition, existing force fields, and an iterative process to tune the parameters to reproduce the experimental data.[23] Despite being very successful in reproducing and helping to interpret many structural and dynamical properties of the breathing motions of MOFs, force-field-based MD simulations have been applied to only a handful of selected structures. From a simulation point of view, the lack of suitable force fields and the effort involved in developing new ones are to blame for this. These problems may be avoided by using DFT-based ab initio molecular dynamics (AIMD) simulation techniques (also called DFT-MD or first-principles MD).[38−40] Since the finite-temperature dynamics is developed with forces obtained directly from first-principles electronic structure calculations made "on the fly", AIMD simulations in principle allow an accurate and unbiased investigation of the chemical processes of interest. In addition, they can be more predictive than the force-field approach, mainly because predefined force fields can be expected only to reproduce the chemical events against which they were parametrized prior to the simulations. Consequently, AIMD simulations have been used successfully in multiple fields of chemistry.[41−45] However, their application to the field of MOFs is still rare.[20,46,47]

In this contribution, we probe and so provide insights into the temperature- and CO_2-adsorption-related breathing phenomena of MIL-53(Sc) by means of AIMD simulations and in situ synchrotron X-ray powder diffraction (XRPD) experiments. As stated above, MIL-53(Sc) has been studied less than its counterparts MIL-53(Cr) and MIL-53(Fe), and its complex structural transformations, which are different from those of the Cr and Fe forms, have yet to be fully measured or understood.[11,14] The MIL-53(Sc) material was therefore an ideal subject for a joint computational AIMD and experimental XRPD study that is the first of its kind. First, we demonstrate a modeling scheme based on AIMD simulations that not only enables a correct prediction of the structural changes of MIL-53(Sc) in response to temperature variations but also provides a molecular-level explanation for them. Then, through a synergetic combination of AIMD simulations and experimental evidence, we determine and elucidate the structural transformations upon CO_2 adsorption and explain features of the experimental diffraction pattern that only MD simulations of this type can predict directly.

2. RESULTS AND DISCUSSION

2.1. Structural Response to Temperature Variations at Zero Guest-Molecule Loading. In a previous work,[14] some of us reported the novel *cp* structural form of MIL-53(Sc) formed upon removal of the guest molecules. Interestingly, the evacuated structure exhibited unusual thermal behavior. The framework underwent a gradual expansion of the unit cell in response to increasing temperature until it changed symmetry from $P2_1/c$ to $C2/c$ at 623 K. The structures obtained at different temperatures were successfully refined against the XRPD patterns in the same work. Because of the availability and, more importantly, the subtlety of the structural changes caused simply by varying the temperature, these experimental structures provide an ideal test case for critically assessing our computational approach. To mimic the experiments in silico, the as-prepared MIL-53(Sc) containing DMF solvent molecules[11] was used as the starting configuration for the framework. The DMF molecules were removed from the framework prior to the simulations, analogous to the activation in the experiment. This structure, denoted as MIL-53(Sc)-*DMF(removed)*, was then used as a starting structure for AIMD simulations performed at three temperatures, namely, 100, 293, and 623 K, which were among the ones investigated experimentally.[14] All of the AIMD-simulated structures reported here were generated by averaging the last portion of the AIMD trajectory (after equilibration) followed by an energy minimization at 0 K in conjunction with the time-averaged unit cell parameters. The computational procedures used to produce these structures are detailed in the Supporting Information (SI). The simulated cell parameters and their standard deviations are given in Table 1, together with the corresponding values from the experiments (in parentheses).[14] For comparison, the parameters for the starting configuration in these AIMD simulations, MIL-53(Sc)-*DMF(removed)*, are also included in Table 1 (in parentheses) to illustrate the significant structural changes observed between the start and finish of the AIMD simulations. The atomic positions are provided in the SI. Table 1 shows that the agreement between the simulated and experimental unit cells is very good for all three temperatures investigated (also see Figure S7 in the SI for comparison of the XRPD patterns). The discrepancies are very small and in most cases within the limits of statistical error. A comparison of selected bond distances and angles from the simulations and experiments is given in Table S4 in the SI.

In both the experiments and the simulations, remarkable cell volume reductions were observed upon removal of the DMF molecules from the as-prepared framework; for instance, the structure shrank by as much as 35% at 100 K. Moreover, the AIMD trajectories suggested that the structural contractions at

dx.doi.org/10.1021/ja403453g | J. Am. Chem. Soc. 2013, 135, 15763−15773

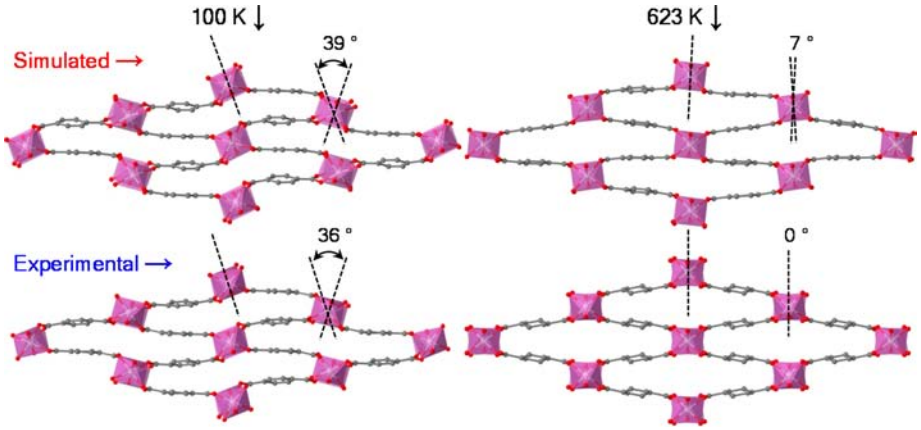

Figure 2. Comparison of the rotation of the Sc hydroxide chains in the (top) AIMD-simulated and (bottom) experimental structures at (left) 100 and (right) 623 K. Dashed lines represent the planes of the infinite Sc–μ_2-O–Sc chains. H atoms have been omitted for clarity.

all three temperatures occurred almost immediately after the simulations started, implying that the as-prepared structure with DMF removed is thermodynamically unfavorable. It is also clear from the standard deviations in Table 1 that considerably larger fluctuations in the simulated cell parameters are associated with the structure at 623 K and that, on the whole, higher temperatures produce larger-amplitude fluctuations (also see Figure S6 in the SI). This observation is of course in accordance with thermodynamic principles.

Besides the gradual expansion of the structure, rotation of the chains of $ScO_4(OH)_2$ octahedra around their long axes in response to increasing temperature was observed both experimentally and computationally for MIL-53(Sc). The extent of rotation can be quantified using the angle formed between the two planes defined by the two Sc–μ_2-O–Sc groups (shown as dashed lines in Figure 2). This angle is 0° in the as-prepared framework structure, MIL-53(Sc)-*DMF-(removed)*, the starting configuration for all three simulations. Experimentally, the angles were found to be 36 and 0° for the structures at 100 and 623 K, respectively (Figure 2). As clearly shown in Figure 2, the AIMD simulations were able to capture almost quantitatively the rotations of the Sc hydroxide chains observed experimentally at the different temperatures in addition to the accurate reproduction of the cell expansions seen in Table 1. As suggested by these correct predictions of the various MIL-53(Sc) structures, our AIMD-simulation-based modeling approach might serve as a means to predict the response of other forms of MIL-53(Sc) and other MOF structures to temperature. However, as with all simulation methods, care must be taken to ensure that the computational procedure is robust. A full validation of the simulation parameters chosen in this work is provided in the SI.

It is also worth noting that the AIMD simulations yielded the correct MIL-53(Sc) structures at the various temperatures without any input based on prior knowledge of the target structures. This level of predictive ability cannot be easily achieved by computational approaches based on energy minimization at 0 K. Therefore, these results show that the entropic effects resulting from molecular motion are successfully included in the AIMD approach. Furthermore, the AIMD simulations provided a dynamic picture on the molecular level that can help in interpreting the unit cell evolution with increasing temperature. In the AIMD simulations, we observed significantly larger rotational and vibrational movements of the phenyl rings of the terephthalate ligands of the framework at 623 K. The length of the ligand is almost invariant upon deformation. Thus, in order to accommodate these large movements of the phenyl rings, the two Sc hydroxide chains corresponding to the short diagonal of the rhombic cross section of the channel have to move away from each other. At the same time, they continue to rotate until they become parallel to each other, ultimately resulting in unit cell expansion and the higher symmetry adopted by the solid at 623 K. Interestingly, despite the large movements of the phenyl rings observed in our simulation at 623 K, no complete "flipping" of the rings was found in the ca. 20 ps trajectory (nor was it observed at lower temperatures). Although the time frame may be too short to establish conclusive evidence, our simulations suggest that flipping may be prevented (probably by sterics) in the less-open forms of MIL-53(Sc), which agrees well with our recent ^{2}H NMR data for the solid measured at 400 K.[48]

As a further step to elucidate the structural response of MIL-53(Sc) to temperature variations, energetic information was extracted from the simulations. The potential energies of the three energy-minimized, time-averaged AIMD structures are given in Table 2, together with that of the starting structure

Table 2. Calculated Potential Energies and Volumes for Various MIL-53(Sc) Framework Structures[a]

structure	ΔE (kJ mol^{-1})	ΔV (Å^3)
MIL-53(Sc)-*cp*(100 K)	0.0	0.0
MIL-53(Sc)-*cp*(293 K)	3.4	26.7
MIL-53(Sc)-*vnp*(623 K)	194.6	292.6
MIL-53(Sc)-*DMF(removed)*	359.6	935.0

[a]Potential energies (ΔE) and volumes (ΔV) were calculated using MIL-53(Sc) frameworks consisting of eight $ScO_4(OH)_2$ units. For each framework, the two values are reported with respect to those for the MIL-53(Sc)-*cp* structure simulated at 100 K. The potential energies were determined by single-point calculations in which the same exchange–correlation grid (constant density of grid points) was used (see the SI for details).

(calculation details are provided in the SI). These values unambiguously confirm that the *cp* structure is indeed energetically favored, corroborating the experimental observation that the solid contracts to adopt the *cp* form upon removal of the guest molecules (water or DMF) from the framework.[11,14] The data in Table 2 also show that there is a correlation between the potential energy and the volume of the

dx.doi.org/10.1021/ja403453g | J. Am. Chem. Soc. 2013, 135, 15763–15773

framework, indicating that the structure becomes increasingly energetically unfavorable as it expands.

The influence of dispersion (or van der Waals) interactions on the MIL-53(Sc) structure needs to be emphasized. A complementary AIMD simulation starting with the *cp* structure (obtained at 100 K with dispersion-corrected DFT a priori) was performed at 100 K employing only DFT, which is known to account poorly for dispersion interactions.[49−51] It was found that the initial *cp* framework gradually opened and the unit cell volume increased by 30% within 3 ps in the AIMD simulation (Figure S8a in the SI), clearly demonstrating that the dispersion interactions play a pivotal role in maintaining the *cp* structure. The importance of dispersion interactions in determining the MIL-53(Sc) structure is in good agreement with the findings for other flexible MOFs.[20,36,52]

Figure 3 provides a structural basis for understanding the relative stabilities of the *cp* and *vnp* structures. In the *cp* structure (at both 100 and 293 K), the two opposite Sc hydroxide chains corresponding to the short diagonal of the rhombic cross section of the channel are present in an energetically favorable conformation. That is, the hydrogen atom of every hydroxyl group interacts strongly with the nearest oxygen atom of the carboxylate group belonging to the opposite chain. The interatomic distances are 2.05 and 2.15 Å at 100 and 293 K, respectively. In contrast, the formation of such strong and directional hydrogen bonds does not occur in the *vnp* structure (the distance between the pair is 3.8 Å) because of the different alignment of the chains at 623 K compared with the configuration in the *cp* structure (Figure 3). Therefore, the predominant hydrogen bonds formed between the two opposite inorganic chains give rise to large intraframework interactions that in turn cause the *cp* structure to be more stable than the *vnp* structure (Table 2). This energetic information complements the dynamic picture of the structural transformation with changing temperature obtained from the AIMD trajectories in explaining why the *vnp* structure can be realized only at much higher temperatures. The larger variations and rotations within the framework (larger kinetic energies) resulting from the higher temperature help to overcome the strong intraframework interactions present in the *cp* form and eventually stabilize the structure in a relatively high potential energy configuration (i.e., *vnp*).

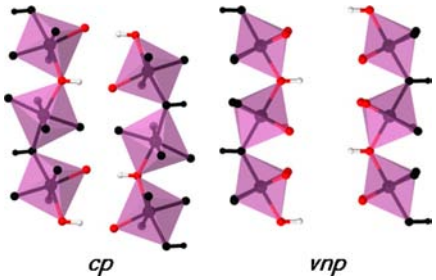

Figure 3. Illustration of the different conformations of the two opposite Sc hydroxide chains in the *cp* and *vnp* forms of MIL-53(Sc). The hydroxyl groups in the central channel and their nearest oxygen atoms of the carboxylate groups belonging to the opposite chain are color coded (white, hydrogen; red, oxygen).

2.2. Structural Response to CO_2 Adsorption at 196 K. *Adsorption Isotherm and in Situ XRPD Patterns.* The previously reported CO_2 adsorption behavior of dehydrated MIL-53(Sc) at 196 K[11] is shown in Figure 4a. In the adsorption branch of the isotherm, negligible amounts of CO_2 are adsorbed up to 0.05 bar. After that, a first step with adsorption of 2−3 mmol g^{-1} is observed, followed by a second step (starting at ca. 0.75 bar) to an uptake of ca. 13 mmol g^{-1}. The in situ XRPD patterns collected on the MIL-53(Sc) sample during CO_2 adsorption at 196 K (Figure 4b) show a remarkable phase evolution of the structure as a function of the CO_2 pressure. The initial structure after outgassing is the *cp* form, which has no apparent porosity to accommodate any measurable amount of CO_2. This is evident from both the adsorption isotherm and the pattern collected at 0.03 bar, which is largely identical to the one for the starting, evacuated solid. As the partial pressure of CO_2 is increased, characteristic XRPD peaks appear at the same pressure regions where the steps in the adsorption isotherm can be observed, displaying a clear correlation between the structural transformations and the amounts of CO_2 adsorbed. At 0.148 bar, corresponding to the beginning of the first plateau in the adsorption branch, a new XRPD signature can be observed, and it continues to be distinguishable up to higher pressures. The uptake of 2−3 mmol g^{-1} might be accommodated by either an *int* form where half of the channels are partially open and the others are closed (Figure 1c) or by an *np* form where all of the channels are partially open (Figure 1d). It should be noted that both forms are observed for MIL-53(Fe) with CO_2 adsorbed.[13] Further investigations were conducted to determine the structural form and are discussed in detail below. After this initial period of low

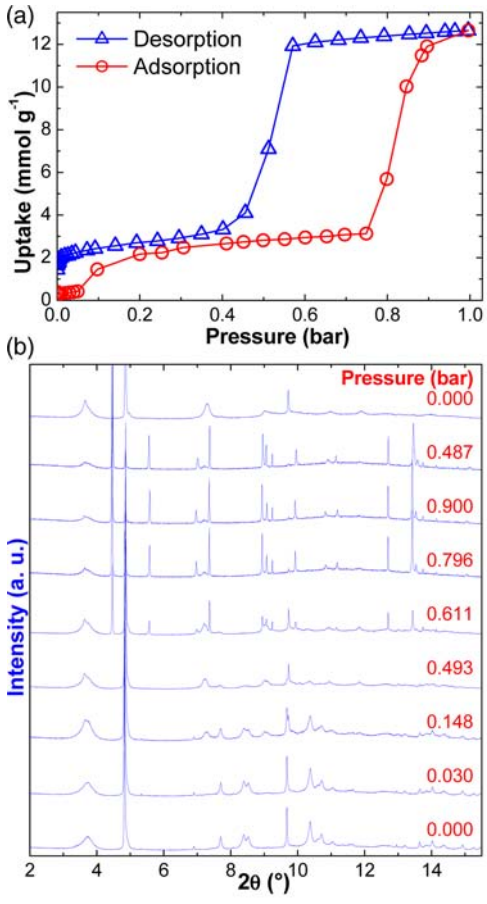

Figure 4. Adsorption of CO_2 on dehydrated MIL-53(Sc) at 196 K as followed by XRPD: (a) adsorption and desorption isotherms of CO_2; (b) variation of the XRPD patterns with CO_2 pressure.

dx.doi.org/10.1021/ja403453g | J. Am. Chem. Soc. 2013, 135, 15763−15773

uptake (2−3 mmol g^{-1}), the second step happens in a much narrower pressure region, and the complete filling of the pores leads to a new structural phase, as suggested by the XRPD patterns at the high pressures. However, the existence of the high-pressure form is notably as a mixture with the other forms observed at the lower pressures. The coexistence of multiple crystallites is similar to the previously reported structures of MIL-53(Fe) upon adsorption of C_2−C_4 alkanes.[16] Interestingly, although the XRPD patterns show reversible phase transitions upon desorption, the structure observed at the first plateau of the adsorption isotherm rather than the *cp* form was retained in the final, outgassed solid. This somewhat surprising result suggests that a longer evacuation time (and possibly a more aggressive procedure) may be needed to reactivate the solid fully.

MIL-53(Sc) Structure at Low CO_2 Loadings. Unambiguous indexing of the pattern at 0.493 bar proved unsuccessful because of significant peak broadening in the experimental pattern (Figure 4b). Since the patterns at higher loadings showed clear evidence for the high-pressure form as a highly crystalline phase, there is no indication that the broadening was a result of beam damage or other degradation. Thus it is more likely to be a structural feature associated with a lowering of crystallographic symmetry. Rietveld refinement using starting literature models, including those of MIL-53(Sc), could not be performed, as the ambiguity in the unit cell parameters and the broadened features of the experimental pattern meant that a suitable model for refinement could not be found. On the other hand, conventional computational approaches based on energy minimization could not be used to assist the structure determination because they rely on prior knowledge of both the unit cell parameters and a starting configuration for the target structure.[13,53,54] Here, we circumvented these restrictions by using AIMD simulations, whose ability to predict structural changes in MIL-53(Sc) in response to temperature variations we have already demonstrated. The MIL-53(Sc)-*DMF-(removed)* structure was again used as the starting configuration for the framework, while the initial CO_2 positions were generated by grand-canonical Monte Carlo (GCMC) simulations (details are given in the SI).[30] As MIL-53(Sc) exhibits the *cp* form after activation, from a simulation standpoint two scenarios regarding the pore-opening mechanism exist. That is, CO_2 adsorption occurs in either half or all of the channels, leading to the *int* or *np* topology, respectively. No conclusive evidence could be established at this stage to verify these structural assignments. Therefore, both hypotheses were tested computationally in parallel (see the SI). The final energy-minimized, time-averaged AIMD structure for the MIL-53(Sc)-*int* form has a triclinic setting (space group *P*1) with simulated lattice parameters a = 20.658 ± 0.152 Å, b = 21.211 ± 0.170 Å, c = 7.413 ± 0.093 Å, α = 92.055 ± 0.830°, β = 88.335 ± 0.547°, and γ = 38.051 ± 0.445°. The topology of the *int* phase is characterized by two sets of diamond-shaped channels with different pore sizes (open and closed), doubling the number of atoms in the unit cell of the as-prepared structure (Figure 5a). The structure corresponding to the *np* topology is discussed in detail in the SI.

First, it is clear from Figure 5b that the experimental XRPD pattern corresponding to the first plateau of the CO_2 adsorption isotherm compares well to the simulated pattern based on the *int* structure, thus confirming that MIL-53(Sc) adopts this form rather than the *np* form (the corresponding comparison of XRPD patterns is shown in Figure S10 in the SI). Furthermore, the *int* phase can be clearly identified in the experimental patterns for pressures ranging from 0.148 to 0.900 bar and during the evacuation (Figure 4b). This *int* form induced by adsorption of CO_2 in only half of the channels (Figure 5a) is, as expected, similar to the hydrated MIL-53(Sc) and MIL-53(Fe)-*int* structures, although it differs in crystallographic detail. It should be noted that the MIL-53(Sc)-*int* structure is stable during CO_2 adsorption, as opposed to the metastable MIL-53(Fe)-*int* structure or the soft mode observed in the Cr solid.[12,16,24] Remarkably, the AIMD simulation suggests a possible explanation for the strong, anisotropic broadening of the experimental XRPD peaks, which hindered the application of more conventional approaches to solving the structure. Figure 5b shows that the pattern for the averaged structure (i.e., the energy-minimized, time-averaged *int* structure illustrated in Figure 5a) gives all of the characteristic peaks observed in the experimental pattern, but the peaks are too narrow, even though the broadening used in the pattern simulation was the same as used for the *lp* form. Averaging a series of patterns based on the snapshots taken during the AIMD simulation (shown in Figure S9 in the SI) yielded an even better agreement with the experimental pattern. Therefore, the anisotropically broadened features of the experimental patterns may be interpreted as a result of the motion and disorder of the adsorbent−adsorbate structure identified by the AIMD simulation. In summary, framework dynamics, which often causes a loss of long-range order and hence broad peak shapes, has been shown to make structure determination difficult by diffraction on its own.[21,55] Here, the averaged pattern is effectively a more realistic representation of the disordered macroscopic sample and thus is in better agreement with the experimental XRPD pattern. In contrast, the averaged structure is an idealized model that is more "crystalline" than the experimental sample, displaying narrower and sharper peaks.

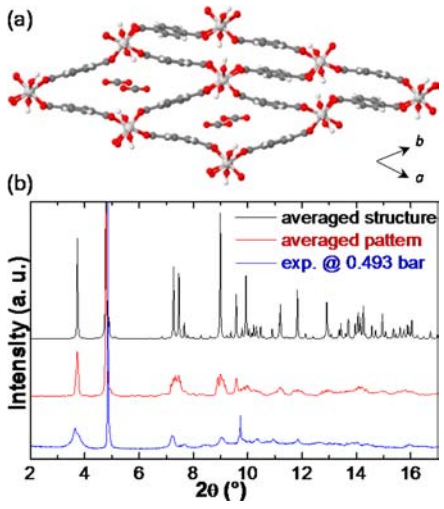

Figure 5. AIMD-simulated MIL-53(Sc)-*int* structure for a CO_2 loading of 2.2 mmol g^{-1}. (a) Unit cell viewed down the channel direction. (b) Comparison of the experimental XRPD pattern collected at a CO_2 pressure of 0.493 bar with two simulated patterns. The "averaged structure" pattern (in black) was calculated on the energy-minimized, time-averaged AIMD structure shown in (a), while the "averaged pattern" (in red) was generated by averaging a series of patterns based on snapshot structures from the same AIMD trajectory used to obtain the time-averaged structure.

dx.doi.org/10.1021/ja403453g | J. Am. Chem. Soc. 2013, 135, 15763−15773

A close inspection of the conformations of the CO_2 molecules located in the open channels of the *int* structure reveals the microscopic adsorption mechanism. Figure 5a shows that the CO_2 molecules are aligned with the long diagonal of the rhombic cross section of the channel and are positioned at the center of the pore, interacting strongly with the hydroxyl groups of the two opposite Sc hydroxide chains corresponding to the short diagonal of the rhombus. The CO_2 molecules are closely "stacked" along the channel and are almost parallel to each other, forming a zigzaglike chain of CO_2 along the channel direction (Figure 6a). Every CO_2 molecule is slightly tilted and displaced to favor a conformation in which an oxygen atom of each CO_2 molecule "pulls" the carbon atom of a neighboring CO_2 molecule.

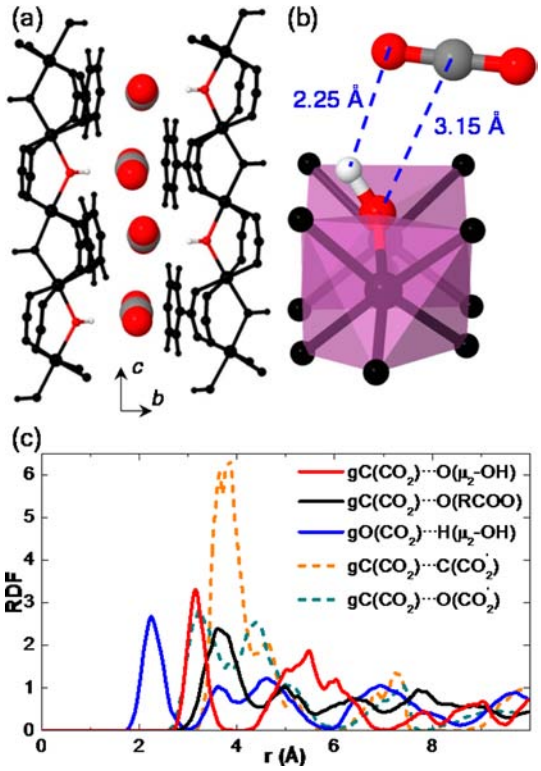

Figure 6. AIMD-simulated MIL-53(Sc)-*int* structure for a CO_2 loading of 2.2 mmol g^{-1}. (a, b) Views of (a) the partially open channels and (b) the double interaction between a CO_2 and a hydroxyl group of the framework. Atoms in the CO_2 molecules and hydroxyl groups are color coded: white, hydrogen; gray, carbon; red, oxygen. (c) Radial distribution functions computed over the last 10 ps of the AIMD simulation.

Radial distribution functions (RDFs)[56] were utilized to characterize time-resolved conformational changes of the adsorbed CO_2 molecule with respect to other CO_2 molecules and the framework (Figure 6c). The characteristic distance between the carbon atoms of two adjacent CO_2 molecules, $C(CO_2)\cdots C(CO_2')$, is 3.65 Å, measured by the first distinct peak of the RDF for the pair. Likewise, the RDF plotted for the $C(CO_2)\cdots O(CO_2')$ pair confirms the close proximity by displaying the first peak centered at 3.30 Å. These short distances between adjacent CO_2 molecules along the channel give rise to strong CO_2-CO_2 interactions. These observations from our AIMD simulations are in line with the joint experimental and theoretical investigation of CO_2 adsorption in MIL-53(Cr) reported previously.[31] However, the distances between neighboring CO_2 molecules in MIL-53(Sc) are larger than the ones observed in the case of MIL-53(Cr), where $C(CO_2)\cdots C(CO_2')$ and $C(CO_2)\cdots O(CO_2')$ were 3.40 and 3.15 Å, respectively. This might be explained partly by the larger *c* dimension of the MIL-53(Sc) unit cell resulting from the larger ionic radius of Sc^{3+}.

More significantly, our AIMD simulations show the formation of electron donor−acceptor (EDA) complexes between the CO_2 molecules and the framework. As illustrated in Figure 6a, each adsorbed CO_2 molecule is situated in close proximity to a hydroxyl group. The CO_2 and the hydroxyl group are "bridged" by a double interaction consisting of the $C(CO_2)\cdots O(\mu_2\text{-OH})$ and $O(CO_2)\cdots H(\mu_2\text{-OH})$ interactions (Figure 6b), as confirmed by the characteristic peaks centered at 3.15 and 2.25 Å, respectively, in the corresponding RDFs. Moreover, the fact that the $C(CO_2)\cdots O(\mu_2\text{-OH})$ distance (3.15 Å) is shorter than the $C(CO_2)\cdots O(RCOO)$ distance (3.55 Å) demonstrates that the carbon atom of the CO_2 molecule interacts preferentially with the oxygen atom of the hydroxyl group over that of the carboxylate group of the framework. In other words, the EDA complex is formed between $C(CO_2)$ as the electron acceptor and $O(\mu_2\text{-OH})$ as the electron donor. Our AIMD simulations thus provide the first evidence concerning the nature of the strong CO_2−framework interactions in the MIL-53(Sc)-*int* structure. The location of the CO_2 molecules relative to the hydroxyl groups of the framework (Figure 6) is similar to that for the $C(CO_2)\cdots O(\mu_2\text{-OH})$ EDA complexes reported for CO_2 adsorption in MIL-53(Cr) and nonfunctionalized MIL-53(Fe).[13,31,57] However, further experimental investigations such as IR spectroscopic measurements are necessary to judge the accuracy of this modeling prediction.[57] The strong CO_2-CO_2 interactions present in the *int* structure are essential for facilitating the observed $C(CO_2)\cdots O(\mu_2\text{-OH})$ EDA complexes (see the further discussion in the SI). This EDA-related phenomenon has been explored by several DFT studies on various MIL-53 solids.[13,31] In those studies, the CO_2 molecule was typically placed inside the framework initially by the simulator. Different CO_2 configurations relative to the framework were then examined by energy minimization calculations at 0 K, in which we would not normally expect to see dramatic steric changes. In contrast, our simulations arrived at the final configurations starting from a completely different picture, as clearly demonstrated by the structural evolution of MIL-53(Sc)-*int* during the course of the AIMD simulation given in the SI. In passing, we note that the dispersion interactions were again found to be crucial for stabilizing the *int* structure. Figure S8b in the SI shows that the volume of the CO_2-loaded framework increased by more than 60% within 3 ps in the AIMD simulation when dispersion corrections were not applied to the DFT calculations.

MIL-53(Sc) Structure at High CO_2 Loadings. The structural phase observed at high CO_2 pressures (0.611−0.900 bar) was also determined by AIMD simulations as described in the SI. The final energy-minimized, time-averaged MIL-53(Sc)-*lp* structure has an orthorhombic unit cell with lattice parameters $a = 7.354 \pm 0.100$ Å, $b = 17.155 \pm 0.112$ Å, $c = 13.442 \pm 0.068$ Å, $\alpha = 90.000 \pm 0.580°$, $\beta = 90.000 \pm 0.561°$, and $\gamma = 90.000 \pm 0.546°$, in very good agreement with the experimentally indexed orthorhombic *Imma* cell with parameters $a = 7.310(1)$ Å, $b = 17.029(2)$ Å, and $c = 13.504(1)$ Å.

In parallel, since the lattice parameters of the *lp* structure were known from the experiment, we used them to identify the

dx.doi.org/10.1021/ja403453g | J. Am. Chem. Soc. 2013, 135, 15763−15773

atomic positions of the framework atoms by applying a procedure based on molecular energy minimization calculations, as explained previously.[58−60] Thereafter, we included and optimized the positions of the adsorbed CO_2 molecules using GCMC simulations (full details are given in the SI). Figure 7 compares the experimental XRPD pattern collected at

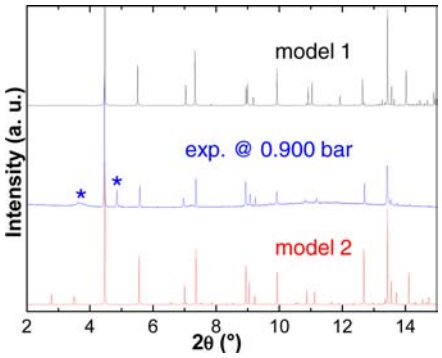

Figure 7. Comparison of the experimental XRPD pattern collected at a CO_2 pressure of 0.900 bar with the patterns for two computational *lp* models: model 1 was realized by AIMD simulations, and model 2 was generated through a combination of GCMC simulations and energy minimizations in conjunction with the experimental unit cell. Diffraction peaks marked with * indicate residual MIL-53(Sc)-*int* and were excluded when fitting the MIL-53(Sc)-*lp* pattern and comparing with the simulated patterns. Model 2 results in a slightly better agreement with the experimental pattern, as R_{wp} values of ca. 10% and ca. 8% were obtained for models 1 and 2, respectively.

a CO_2 pressure of 0.900 bar with simulated patterns based on the two computationally anticipated structures (models 1 and 2). Both modeling approaches (i.e., the AIMD simulation and the energy minimization in conjunction with the experimental unit cell) were able to assist in determining the structure of the *lp* phase. While the energy-minimization-based approach is computationally much less expensive and is therefore the obvious choice when the cell parameters are known experimentally, the computationally more expensive AIMD method is the only viable option if the experimental cell parameters are not known a priori.

The AIMD simulations indicate that 16 CO_2 molecules can be accommodated per unit cell for the *lp* structure, while the maximum uptake observed experimentally is ca. 13 mmol g^{-1} (corresponding to ca. 12 CO_2 molecules per unit cell). This suggests that a fraction of the pores in the solid remains closed even at this high uptake. This is in line with the in situ XRPD measurements (Figure 4b), which suggest the coexistence of the *int* and *lp* phases. It can thus be concluded that during CO_2 adsorption two structural transformations occur (i.e., *cp* → *int* and *int* → *lp*) and that MIL-53(Sc) adopts a mixture of two phases over a wide pressure range, probably as a result of kinetic restrictions.

We note that in contrast to the clear establishment of C(CO_2)···O(μ_2-OH) EDA complexes in the *int* form, where each CO_2 molecule is strongly "anchored" by a hydroxyl group (Figure 6), the situation in the *lp* form is markedly different. The *lp* simulation indicates that C(CO_2) no longer exclusively interacts with O(μ_2-OH) but rather shows more frequent preferential arrangements with O(RCOO). In addition, the interatomic distances of the pairs defined in Figure 6c are consistently smaller than the ones in the *int* form because of the condensation of CO_2 in the pores at this high loading (16 CO_2 molecules per unit cell). These observations are in line with findings for the adsorption of small gas molecules in *lp* MIL-53(Cr) and MIL-47.[33,35,61,62]

Energetics of the Different Forms and Structural Transformations. Further fundamental insight into the different structural forms of MIL-53(Sc) upon CO_2 adsorption can be obtained by analyzing the potential energies of the framework structures and pore-opening energies for the structural transformations. Table 3 summarizes the potential energies

Table 3. Potential Energies and Volumes for the Empty MIL-53(Sc) Structures and Pore-Opening Energies for the Different Structural Transformations

Potential Energies and Volumes		
structure	ΔE (kJ mol^{-1})[a]	ΔV (Å^3)[a]
MIL-53(Sc)-*cp*	0.0	0.0
MIL-53(Sc)-*int*[b]	146.6	334.1
MIL-53(Sc)-*np*[b]	318.9	661.6
MIL-53(Sc)-*lp*[b]	644.5	1733.5
Pore-Opening Energies		
structural transformation	ΔE_{open} (kJ mol^{-1})[c]	
cp(0.0) → *int*(2.2)	−77.3	
cp(0.0) → *np*(2.2)	+95.8	
int(2.2) → *int*(3.3)	−57.7	
int(2.2) → *np*(3.3)	+89.6	

[a]Potential energies (ΔE) and volumes (ΔV) for frameworks containing eight $ScO_4(OH)_2$ units relative to those of the *cp* structure simulated at 100 K. [b]Prior to the calculation, the CO_2 molecules were removed. [c]Energy required for the particular structural transformation. The framework topology is given in italic type, and the CO_2 loading in mmol g^{-1} is given in parentheses. All of the energies were determined by single-point calculations in which the same exchange−correlation grid (constant density of grid points) was used (see the SI for details).

determined for the empty frameworks (i.e., the CO_2 molecules were not included in the calculations; computational details can be found in the SI). On the basis of these results and the potential energies of the *vnp* framework and the *DMF(removed)* as-prepared framework reported in Table 2, it is clear that the *cp* structure is indeed the global minimum for a given temperature, as the energy of any other form is greater than that of the *cp* form (i.e., $\Delta E > 0$). It can also be seen that the more open the structure is, the more energetically unfavorable it becomes (Tables 2 and 3). This decreasing structural stability with expansion of the framework can be largely attributed to the decrease in dispersion interactions as the structure becomes increasingly less dense (see Figure S13 in the SI). The only outlier is the *int* structure, which is more stable than the *vnp* structure even though it has a larger cell volume. This can be rationalized by the fact that the *int* structure has half of its channels remaining in the *cp* form, which has a much lower energy than the *vnp* form.

It should be emphasized that the calculated potential energy of a particular form of MIL-53(Sc) is the internal energy at 0 K for the particular framework configuration induced by changes in either temperature or CO_2 uptake. The energetic information may be indicative of the relative stabilities of the different empty framework structures but does not necessarily convey information on the actual structural transformations in response to an external stimulus. To be specific, in the absence of guest molecules, increasing the temperature converts the structure from the *cp* form to the *vnp* form rather than the *int*

dx.doi.org/10.1021/ja403453g | J. Am. Chem. Soc. 2013, 135, 15763−15773

form. The reason why the *vnp* form rather than the *int* form is adopted by the solid at 623 K is that the half-closed structure would restrict large motions that are inevitable at this high temperature. This is in essence the same as stating that the *vnp* form is observed in place of the *cp* form at 623 K even though the *cp* phase has the lower potential energy.

The relative stabilities of the various structural forms therefore allow us to interpret the different breathing behaviors of the MIL-53 solids upon evacuation. Removing guest molecules from the MIL-53(Sc) framework always results in the *cp* structure (or the *vnp* form if the solid is heated up to 623 K) because it is the most energetically favored. In contrast, outgassed MIL-53(Cr) adopts the *lp* phase, in line with a previous theoretical study in which the dehydrated *lp* structure was found to be lower in energy than its *np* counterpart.[28]

For particular amounts of adsorbed CO_2, the energies required for different structural transformations to accommodate the uptake were determined in order to elucidate the phase evolution in response to CO_2 adsorption (Table 3). As a first approximation, the sorption-induced pore-opening energy (ΔE_{open}) can be estimated from the difference between the energies before and after uptake of a certain amount of CO_2 (calculation details can be found in the SI). The energies needed to open the *cp* structure to form the *int* and *np* topologies are −77.3 and +95.8 kJ mol^{-1}, respectively. The negative pore-opening energy in the former case confirms that formation of the *int* structure can be expected as a result of exposure of MIL-53(Sc)-*cp* to CO_2. In contrast, the large positive value in the case of the *np* structure entails the need for a significant amount of external energy to initiate the pore opening, thus providing further evidence that in the experiment only the *int* structure is formed. To ascertain the preferential structural transformations for further CO_2 adsorption starting from the *int* structure with a loading of 2.2 mmol g^{-1} (four CO_2 molecules per unit cell of the *int* structure), we proceeded to consider a higher uptake of 3.3 mmol g^{-1} (six CO_2 molecules per unit cell of the *int* structure). Two scenarios were investigated: (1) the additional CO_2 adsorption occurred in the already open channels, thus maintaining the *int* topology; and (2) the initially closed channels were opened as a result of the uptake, leading to the *np* topology. A schematic representation of the two structural transformations can be found in Figure S4 in the SI. The pore-opening energies were found to be −57.7 and +89.6 kJ mol^{-1} for the *int*(2.2) → *int*(3.3) and *int*(2.2) → *np*(3.3) transformations, respectively. This indicates that upon CO_2 adsorption the MIL-53(Sc) solid favors saturation of the open channels over opening of closed channels, corroborating the in situ XRPD patterns, which suggested the presence of the *int* phase up to high CO_2 partial pressures.

3. CONCLUSIONS

The breathing behavior of the MIL-53(Sc) solid in response to temperature variations and CO_2 adsorption was probed and elucidated through a joint experimental and computational investigation. The AIMD-simulation-based approach was first demonstrated to predict accurately the *cp* and *vnp* forms of MIL-53(Sc) at three different temperatures. By a combination of the same modeling approach with in situ XRPD experiments, the structural transformations of MIL-53(Sc) upon CO_2 adsorption were studied. The significantly broadened XRPD peaks of the phase at a CO_2 pressure of 0.493 bar posed a hurdle to structure determination by commonly adopted methods such as Rietveld refinement or energy minimization. We therefore carried out AIMD simulations that successfully facilitated the determination of the MIL-53(Sc)-*int* structure for the phase (at 0.493 bar) corresponding to the first plateau of the CO_2 adsorption isotherm (2−3 mmol g^{-1}). While AIMD simulations were the only viable choice to identify the *int* structure, the *lp* phase with the unit cell indexed experimentally was successfully solved by both the AIMD- and energy-minimization-based approaches. The latter is of course more computationally efficient and therefore should be used to predict atomic positions of the structure when the unit cell parameters are available. Apart from assisting the structure determinations, the AIMD simulations further provided molecular-level dynamic and energetic information that helped to reveal the nature of the structural responses of MIL-53(Sc) to the external stimuli.

This work is to the best of our knowledge the first systematic demonstration of the application of AIMD simulations to study the flexibility of MOFs upon temperature variation and adsorption uptake. A special focus was on showcasing the applicability of the methodology to assist with structure determinations when the more conventional techniques fail. Since the energies and forces are calculated by a chosen QM method "on the fly", AIMD simulations are likely to permit computational investigation of a larger number of flexible MOFs than force-field-based approaches. For example, the effect of the nature of the metal on the breathing of the MIL-53 solids with different metals is not yet fully understood. On the basis of correct reproductions of the different breathing behaviors by AIMD simulations, the first-principles descriptions of the MIL-53 variants obtained from such simulations will increase our understanding of the phenomena. Last but not least, as demonstrated by the successful identification of the MIL-53(Sc)-*int* structure in this work, AIMD simulations are predictive and are certainly worth exploring in a wider context in the field of MOFs and other flexible and dynamic microporous solids.

4. METHODS

4.1. Experimental Details. The MIL-53(Sc) sample used for the in situ measurements was prepared via the reported method.[11] In a typical reaction, MIL-53 was prepared using a solution of scandium nitrate hydrate, terephthalic acid, pyridine, and DMF in a $Sc(NO_3)_3{\cdot}3H_2O$:H_2BDC:C_5H_5N:DMF molar ratio of 1:1:15:200. The solution was then thoroughly mixed by stirring at room temperature and heated at 463 K for 40 h in a Teflon-lined stainless steel Parr autoclave. Following the reaction, samples were filtered and washed thoroughly with either DMF or ethanol and dried in a drying oven at 323 K. In preparation for the gas loading measurements, samples were ground and packed into 0.7 mm quartz capillaries, and a glass wool plug was inserted to prevent the powder from moving upon evacuation. The capillary was attached to a goniometer head with an attached gas line allowing connection to the pressure control board and turbomolecular pump. Samples of MIL-53(Sc) were activated at 623 K for 10 h in a tube furnace prior to the experiment and again at 373 K under evacuation with the turbomolecular pump to ensure complete removal of guest species from within the pores. Gas was manually dosed into the system in small increments, and the pressure was recorded using the attached gauge. The pressure steps were selected on the basis of the CO_2 adsorption isotherm to gain in situ data for all of the structural forms predicted to occur over

dx.doi.org/10.1021/ja403453g | J. Am. Chem. Soc. 2013, 135, 15763−15773

the course of the isotherm (i.e., the *cp* structure upon activation, an *int* structure at 0.2−0.7 bar, and the fully loaded *lp* form). Data were collected on beamline I-11 at the Diamond Light Source using a position-sensitive detector comprising 18 MYTHEN-II detector modules covering a 2θ range of 0−90° with an angular resolution of 0.005°. Because of the small gaps between detector modules, two data sets were collected 0.25° apart and the data were merged to give a continuous data set. The data sets presented here and used in the Rietveld refinement were merged from two 8 s data collections, which allowed for rapid in situ monitoring of the evacuation, dehydration, and adsorption processes to ensure that the observed changes were completed before continuing.

4.2. Computer Simulations. All of the AIMD simulations and DFT-based geometry optimizations were performed employing DFT (with periodic boundary conditions and *P*1 symmetry) as implemented in the QUICKSTEP[63] module of the CP2K simulation package (http://www.cp2k.org/). Energies and forces were calculated with the Gaussian plane-wave scheme,[63,64] which uses a dual basis set method wherein a linear combination of Gaussian-type orbitals is used to describe the Kohn−Sham molecular orbitals while the electron density is described by an auxiliary plane-wave basis set. A double-ζ valence plus polarization basis set, in conjunction with the relativistic, norm-conserving Goedecker−Teter−Hutter pseudopotentials, was used for all elements other than Sc, which was described using the MOLOPT basis set.[65−68] All of the calculations were done using the Becke−Lee−Yang−Parr (BLYP)[69,70] exchange−correlation functional with semiempirical dispersion corrections to the energies and gradients from the DFT-D3[71] method, unless explicitly stated otherwise. Born−Oppenheimer MD simulations were carried out in the isobaric−isothermal (*NPT*) ensemble (i.e., constant number of particles, pressure, and temperature). In all of the AIMD simulations carried out in this contribution, both the shape and dimensions of the simulation box could vary, and no constraints were applied to any degree of freedom of the system. Extensive details on the computational setup and modeling procedures can be found in the SI.

■ ASSOCIATED CONTENT

Supporting Information

Computational details about the DFT calculations, DFT-based geometry optimization calculations, and AIMD simulations; GCMC simulation details, generic force-field parameters for MIL-53(Sc) and CO_2 atoms, and partial atomic charges for the MIL-53(Sc) framework; AIMD-simulation-based modeling procedures for generating the various structural forms of MIL-53(Sc); details about the calculation of framework potential energies and pore-opening energies; time evolution of the MIL-53(Sc)-*int* structure during the course of the AIMD simulation; description of the MIL-53(Sc)-*np* structure and comparison with the *int* form; and details about the determination of the MIL-53(Sc)-*lp* structure via the energy-minimization-based modeling approach in conjunction with the experimental unit cell parameters. This material is available free of charge via the Internet at http://pubs.acs.org.

■ AUTHOR INFORMATION

Corresponding Author

tina.duren@ed.ac.uk

Notes

The authors declare no competing financial interest.

■ ACKNOWLEDGMENTS

We thank the EPSRC for funding (EP/G062129/1) and Doctoral Prize funding (J.P.S.M.). D.F.-J. thanks the Royal Society for funding through a University Research Fellowship. This work made use of the Edinburgh Compute and Data Facility (ECDF) (http://www.ecdf.ed.ac.uk) and the resources provided by HECToR (http://www.hector.ac.uk), made available through the ECDF. We acknowledge Professor Chiu C. Tang for assistance at beamline I-11 at the Diamond Light Source (DLS) and DLS for beam time.

■ REFERENCES

(1) Zhou, H.-C.; Long, J. R.; Yaghi, O. M. *Chem. Rev.* **2012**, *112*, 673.
(2) Kitagawa, S.; Kitaura, R.; Noro, S.-i. *Angew. Chem., Int. Ed.* **2004**, *43*, 2334.
(3) Férey, G.; Serre, C. *Chem. Soc. Rev.* **2009**, *38*, 1380.
(4) Horike, S.; Shimomura, S.; Kitagawa, S. *Nat. Chem.* **2009**, *1*, 695.
(5) Serre, C.; Millange, F.; Thouvenot, C.; Noguès, M.; Marsolier, G.; Louër, D.; Férey, G. *J. Am. Chem. Soc.* **2002**, *124*, 13519.
(6) Serre, C.; Mellot-Draznieks, C.; Surblé, S.; Audebrand, N.; Filinchuk, Y.; Férey, G. *Science* **2007**, *315*, 1828.
(7) Férey, G.; Serre, C.; Devic, T.; Maurin, G.; Jobic, H.; Llewellyn, P. L.; De Weireld, G.; Vimont, A.; Daturi, M.; Chang, J.-S. *Chem. Soc. Rev.* **2011**, *40*, 550.
(8) Horcajada, P.; Gref, R.; Baati, T.; Allan, P. K.; Maurin, G.; Couvreur, P.; Férey, G.; Morris, R. E.; Serre, C. *Chem. Rev.* **2012**, *112*, 1232.
(9) Loiseau, T.; Serre, C.; Huguenard, C.; Fink, G.; Taulelle, F.; Henry, M.; Bataille, T.; Férey, G. *Chem.—Eur. J.* **2004**, *10*, 1373.
(10) Whitfield, T. R.; Wang, X.; Liu, L.; Jacobson, A. J. *Solid State Sci.* **2005**, *7*, 1096.
(11) Mowat, J. P. S.; Miller, S. R.; Slawin, A. M. Z.; Seymour, V. R.; Ashbrook, S. E.; Wright, P. A. *Microporous Mesoporous Mater.* **2011**, *142*, 322.
(12) Millange, F.; Guillou, N.; Walton, R. I.; Greneche, J.-M.; Margiolaki, I.; Férey, G. *Chem. Commun.* **2008**, 4732.
(13) Devic, T.; Salles, F.; Bourrelly, S.; Moulin, B.; Maurin, G.; Horcajada, P.; Serre, C.; Vimont, A.; Lavalley, J.-C.; Leclerc, H.; Clet, G.; Daturi, M.; Llewellyn, P. L.; Filinchuk, Y.; Férey, G. *J. Mater. Chem.* **2012**, *22*, 10266.
(14) Mowat, J. P. S.; Seymour, V. R.; Griffin, J. M.; Thompson, S. P.; Slawin, A. M. Z.; Fairen-Jimenez, D.; Düren, T.; Ashbrook, S. E.; Wright, P. A. *Dalton Trans.* **2012**, *41*, 3937.
(15) Millange, F.; Serre, C.; Guillou, N.; Férey, G.; Walton, R. I. *Angew. Chem., Int. Ed.* **2008**, *47*, 4100.
(16) Llewellyn, P. L.; Horcajada, P.; Maurin, G.; Devic, T.; Rosenbach, N.; Bourrelly, S.; Serre, C.; Vincent, D.; Loera-Serna, S.; Filinchuk, Y.; Férey, G. *J. Am. Chem. Soc.* **2009**, *131*, 13002.
(17) Hamon, L.; Llewellyn, P. L.; Devic, T.; Ghoufi, A.; Clet, G.; Guillerm, V.; Pirngruber, G. D.; Maurin, G.; Serre, C.; Driver, G.; van Beek, W.; Jolimaître, E.; Vimont, A.; Daturi, M.; Férey, G. *J. Am. Chem. Soc.* **2009**, *131*, 17490.
(18) Yang, Q.; Wiersum, A. D.; Jobic, H.; Guillerm, V.; Serre, C.; Llewellyn, P. L.; Maurin, G. *J. Phys. Chem. C* **2011**, *115*, 13768.
(19) Salles, F.; Maurin, G.; Serre, C.; Llewellyn, P. L.; Knöfel, C.; Choi, H. J.; Filinchuk, Y.; Oliviero, L.; Vimont, A.; Long, J. R.; Férey, G. *J. Am. Chem. Soc.* **2010**, *132*, 13782.
(20) Hoffmann, H. C.; Assfour, B.; Epperlein, F.; Klein, N.; Paasch, S.; Senkovska, I.; Kaskel, S.; Seifert, G.; Brunner, E. *J. Am. Chem. Soc.* **2011**, *133*, 8681.
(21) Rabone, J.; Yue, Y.-F.; Chong, S. Y.; Stylianou, K. C.; Bacsa, J.; Bradshaw, D.; Darling, G. R.; Berry, N. G.; Khimyak, Y. Z.; Ganin, A. Y.; Wiper, P.; Claridge, J. B.; Rosseinsky, M. J. *Science* **2010**, *329*, 1053.
(22) Férey, G. *Z. Anorg. Allg. Chem.* **2012**, *638*, 1897.

(23) Ghoufi, A.; Subercaze, A.; Ma, Q.; Yot, P. G.; Ke, Y.; Puente-Orench, I.; Devic, T.; Guillerm, V.; Zhong, C.; Serre, C.; Férey, G.; Maurin, G. *J. Phys. Chem. C* **2012**, *116*, 13289.
(24) Ghoufi, A.; Maurin, G.; Férey, G. *J. Phys. Chem. Lett.* **2010**, *1*, 2810.
(25) Dubbeldam, D.; Krishna, R.; Snurr, R. Q. *J. Phys. Chem. C* **2009**, *113*, 19317.
(26) Coudert, F.-X.; Mellot-Draznieks, C.; Fuchs, A. H.; Boutin, A. *J. Am. Chem. Soc.* **2009**, *131*, 11329.
(27) Triguero, C.; Coudert, F.-X.; Boutin, A.; Fuchs, A. H.; Neimark, A. V. *J. Chem. Phys.* **2012**, *137*, No. 184702.
(28) Coombes, D. S.; Corà, F.; Mellot-Draznieks, C.; Bell, R. G. *J. Phys. Chem. C* **2008**, *113*, 544.
(29) Triguero, C.; Coudert, F.-X.; Boutin, A.; Fuchs, A. H.; Neimark, A. V. *J. Phys. Chem. Lett.* **2011**, *2*, 2033.
(30) Frenkel, D.; Smit, B. *Understanding Molecular Simulation: From Algorithms to Applications*, 2nd ed.; Academic Press: San Diego, CA, 2002.
(31) Serre, C.; Bourrelly, S.; Vimont, A.; Ramsahye, N. A.; Maurin, G.; Llewellyn, P. L.; Daturi, M.; Filinchuk, Y.; Leynaud, O.; Barnes, P.; Férey, G. *Adv. Mater.* **2007**, *19*, 2246.
(32) Salles, F.; Ghoufi, A.; Maurin, G.; Bell, R. G.; Mellot-Draznieks, C.; Férey, G. *Angew. Chem., Int. Ed.* **2008**, *47*, 8487.
(33) Bourrelly, S.; Moulin, B.; Rivera, A.; Maurin, G.; Devautour-Vinot, S.; Serre, C.; Devic, T.; Horcajada, P.; Vimont, A.; Clet, G.; Daturi, M.; Lavalley, J.-C.; Loera-Serna, S.; Denoyel, R.; Llewellyn, P. L.; Férey, G. *J. Am. Chem. Soc.* **2010**, *132*, 9488.
(34) Salles, F.; Bourrelly, S.; Jobic, H.; Devic, T.; Guillerm, V.; Llewellyn, P.; Serre, C.; Férey, G.; Maurin, G. *J. Phys. Chem. C* **2011**, *115*, 10764.
(35) Hamon, L.; Leclerc, H.; Ghoufi, A.; Oliviero, L.; Travert, A.; Lavalley, J.-C.; Devic, T.; Serre, C.; Férey, G.; De Weireld, G.; Vimont, A.; Maurin, G. *J. Phys. Chem. C* **2011**, *115*, 2047.
(36) Zhang, L.; Hu, Z.; Jiang, J. *J. Am. Chem. Soc.* **2013**, *135*, 3722.
(37) Vanduyfhuys, L.; Verstraelen, T.; Vandichel, M.; Waroquier, M.; Van Speybroeck, V. *J. Chem. Theory Comput.* **2012**, *8*, 3217.
(38) Car, R.; Parrinello, M. *Phys. Rev. Lett.* **1985**, *55*, 2471.
(39) Mark, E. T. *J. Phys.: Condens. Matter* **2002**, *14*, R1297.
(40) Kirchner, B.; di Dio, P. J.; Hutter, J. *Top. Curr. Chem.* **2012**, *307*, 109.
(41) Sieffert, N.; Bühl, M.; Gaigeot, M.-P.; Morrison, C. A. *J. Chem. Theory Comput.* **2013**, *9*, 106.
(42) Kimmel, G. A.; Baer, M.; Petrik, N. G.; VandeVondele, J.; Rousseau, R.; Mundy, C. J. *J. Phys. Chem. Lett.* **2012**, *3*, 778.
(43) Mallik, B. S.; Siepmann, J. I. *J. Phys. Chem. B* **2010**, *114*, 12577.
(44) Schmidt, J.; VandeVondele, J.; Kuo, I. F. W.; Sebastiani, D.; Siepmann, J. I.; Hutter, J.; Mundy, C. J. *J. Phys. Chem. B* **2009**, *113*, 11959.
(45) Poater, A.; Ragone, F.; Correa, A.; Cavallo, L. *J. Am. Chem. Soc.* **2009**, *131*, 9000.
(46) Kanoo, P.; Reddy, S. K.; Kumari, G.; Haldar, R.; Narayana, C.; Balasubramanian, S.; Maji, T. K. *Chem. Commun.* **2012**, *48*, 8487.
(47) Schröder, C. A.; Baburin, I. A.; van Wullen, L.; Wiebcke, M.; Leoni, S. *CrystEngComm* **2013**, *15*, 4036.
(48) Wright, P. A.; Mowat, J. P. S. Unpublished data.
(49) Kristyán, S.; Pulay, P. *Chem. Phys. Lett.* **1994**, *229*, 175.
(50) Cohen, A. J.; Mori-Sánchez, P.; Yang, W. *Chem. Rev.* **2012**, *112*, 289.
(51) Klimeš, J.; Michaelides, A. *J. Chem. Phys.* **2012**, *137*, No. 120901.
(52) Stavitski, E.; Pidko, E. A.; Couck, S.; Remy, T.; Hensen, E. J. M.; Weckhuysen, B. M.; Denayer, J.; Gascon, J.; Kapteijn, F. *Langmuir* **2011**, *27*, 3970.
(53) Surble, S.; Serre, C.; Mellot-Draznieks, C.; Millange, F.; Férey, G. *Chem. Commun.* **2006**, 284.
(54) Devic, T.; Horcajada, P.; Serre, C.; Salles, F.; Maurin, G.; Moulin, B.; Heurtaux, D.; Clet, G.; Vimont, A.; Grenèche, J.-M.; Le Ouay, B.; Moreau, F.; Magnier, E.; Filinchuk, Y.; Marrot, J.; Lavalley, J.-C.; Daturi, M.; Férey, G. *J. Am. Chem. Soc.* **2010**, *132*, 1127.
(55) Stylianou, K. C.; Rabone, J.; Chong, S. Y.; Heck, R.; Armstrong, J.; Wiper, P. V.; Jelfs, K. E.; Zlatogorsky, S.; Bacsa, J.; McLennan, A. G.; Ireland, C. P.; Khimyak, Y. Z.; Thomas, K. M.; Bradshaw, D.; Rosseinsky, M. J. *J. Am. Chem. Soc.* **2012**, *134*, 20466.
(56) Levine, B. G.; Stone, J. E.; Kohlmeyer, A. *J. Comput. Phys.* **2011**, *230*, 3556.
(57) Vimont, A.; Travert, A.; Bazin, P.; Lavalley, J.-C.; Daturi, M.; Serre, C.; Férey, G.; Bourrelly, S.; Llewellyn, P. L. *Chem. Commun.* **2007**, 3291.
(58) Strutt, N. L.; Fairen-Jimenez, D.; Iehl, J.; Lalonde, M. B.; Snurr, R. Q.; Farha, O. K.; Hupp, J. T.; Stoddart, J. F. *J. Am. Chem. Soc.* **2012**, *134*, 17436.
(59) Fairen-Jimenez, D.; Colon, Y. J.; Farha, O. K.; Bae, Y.-S.; Hupp, J. T.; Snurr, R. Q. *Chem. Commun.* **2012**, *48*, 10496.
(60) Bury, W.; Fairen-Jimenez, D.; Lalonde, M. B.; Snurr, R. Q.; Farha, O. K.; Hupp, J. T. *Chem. Mater.* **2013**, *25*, 739.
(61) Bourrelly, S.; Llewellyn, P. L.; Serre, C.; Millange, F.; Loiseau, T.; Férey, G. *J. Am. Chem. Soc.* **2005**, *127*, 13519.
(62) Llewellyn, P. L.; Bourrelly, S.; Vagner, C.; Heymans, N.; Leclerc, H.; Ghoufi, A.; Bazin, P.; Vimont, A.; Daturi, M.; Devic, T.; Serre, C.; Weireld, G. D.; Maurin, G. *J. Phys. Chem. C* **2013**, *117*, 962.
(63) VandeVondele, J.; Krack, M.; Mohamed, F.; Parrinello, M.; Chassaing, T.; Hutter, J. *Comput. Phys. Commun.* **2005**, *167*, 103.
(64) Lippert, G.; Hutter, J.; Parrinello, M. *Mol. Phys.* **1997**, *92*, 477.
(65) Goedecker, S.; Teter, M.; Hutter, J. *Phys. Rev. B* **1996**, *54*, 1703.
(66) Hartwigsen, C.; Goedecker, S.; Hutter, J. *Phys. Rev. B* **1998**, *58*, 3641.
(67) Krack, M. *Theor. Chem. Acc.* **2005**, *114*, 145.
(68) VandeVondele, J.; Hutter, J. *J. Chem. Phys.* **2007**, *127*, No. 114105.
(69) Becke, A. D. *Phys. Rev. A* **1988**, *38*, 3098.
(70) Lee, C.; Yang, W.; Parr, R. G. *Phys. Rev. B* **1988**, *37*, 785.
(71) Grimme, S.; Antony, J.; Ehrlich, S.; Krieg, H. *J. Chem. Phys.* **2010**, *132*, No. 154104.